Towards Deterministic 3D Energy Storage Electrode Architectures via Electrodeposition of Molybdenum Oxide onto CNT Foams

Michael A. Spencer, [a] *Ozkan Yildiz,* [b] *Ishita Kamboj,* [a]

Philip D. Bradford, [b] *& Veronica Augustyn* [a,*]

[a] Department of Materials Science and Engineering, North Carolina State University, 911 Partners Way, Raleigh, NC 27606, USA

[b] Department of Textile Engineering, Chemistry, and Science, North Carolina State University Raleigh, NC 27695, USA

[*] Corresponding author, vaugust@ncsu.edu

KEYWORDS: transition metal oxide, 3D electrode, electrodeposition, aligned CNT, lithium-ion battery

ABSTRACT: Three-dimensional (3D) deterministic design of electrodes could enable simultaneous high energy and power density for electrochemical energy storage devices. The goal of such electrode architectures is to provide adequate charge (electron and ion) transport pathways for high power while maintaining high active material loading (> 10 mg cm^{-2}) for high areal and volumetric capacity. However, it remains a challenge to fabricate such electrodes with processes that are both scalable and reproducible. Towards this end, here we demonstrate how the fabrication of such an electrode is made possible by combining tunable, free-standing, and aligned CNT foams with aqueous electrodeposition of a model intercalation-type transition metal oxide, MoO_3. Morphological characterization including X-ray micro-computed tomography indicates that the obtained composite is homogenous. Electrodes with active mass loading up to 18 mg cm^{-2} reached near-theoretical Li-ion intercalation capacities within 1.7 hours. The highest mass loading electrodes also led to areal and volumetric capacities of 4.5 mAh cm^{-2} and 290 mAh cm^{-3} with 55% capacity retention for charge/discharge times of 10 minutes. Overall, this work demonstrates a scalable, deterministic 3D electrode design strategy using electrodeposition and free-standing, aligned CNT foams that lead to high areal and volumetric capacities and good rate performance due to well-distributed charge transport pathways.

1. INTRODUCTION

Electrochemical energy storage (EES) devices for hybrid/electric vehicles and portable electronics should provide simultaneous high energy and high power density. However, this is typically challenging because energy and power are integrally coupled in EES electrodes, particularly those that utilize transition metal oxides as the active materials. Transition metal oxides (TMOs) can store charge through reversible intercalation reactions of alkali ions such as Li^+,[1,2] which leads to high specific capacities (typically greater than 100 mAh g^{-1}).[3,4] However, in electrodes with commercially-relevant active material loading (> 10 mg cm^{-2}), the limited electronic conductivity and slow solid-state diffusion of Li^+ in most TMOs restrict the gravimetric utilization and rate performance.[5] Mixing micron-scale active materials with conductive carbon additives and polymer binders improves electronic transport to the active material and electrode stability. However, it remains challenging to ensure good contact between the TMO and current collector as well as a high interfacial area between the TMO and the electrolyte at high active material loading. Furthermore, achieving continuous electron and ion transport pathways in a homogeneous slurry becomes challenging when using non-spherical, nanostructured TMOs.[6] These findings necessitate the development of deterministic three-dimensional electrode architectures that optimize electron and ion transport in high mass loading electrodes. Equally necessary is obtaining such electrode architectures via reproducible, controllable, and scalable processes.[7]

The concept behind deterministic energy storage electrode architectures is to control the assembly of matter so that ion and electron pathways are intentionally designed and not subject to randomness.[8] 3D deterministic electrodes typically contain a porous, electronically conductive component coated with an active material.[9–12] Engineering the structure of these composite electrode materials allows control over the electron and ion transport pathways and may enable

fast ion storage kinetics (with typical rates of at least 1*C*, t = 60 min, where *C* is the theoretical capacity of the material) in high active material loading (> 10 mg cm^{-2}) electrodes.[8,13,14] Metal foams and carbon textiles are frequently used as scaffolds due to their high electronic conductivity, good mechanical integrity, and high surface area. Carbon textiles are advantageous due to their lower mass contribution compared to metals, which are much denser.[8] Zhang et al. reported that good electrical contact between a high surface area carbon nanofoam and conformal metal oxide electrodeposits (up to 145 mg cm^{-2}) led to high utilization of active mass and enabled mechanical flexibility.[15] Another study revealed that compression of 3D architected electrodes can remove excess porosity that would otherwise reduce the volumetric performance.[16] Reversibly-compressible CNT sponges were loaded with Co_3O_4 and compressed up to 90% in a Li-ion battery coin cell with little change in the active material utilization and rate performance. The performance at high Co_3O_4 mass loading (up to 14.3 mg cm^{-2}) and rates >1*C* was attributed to the retention of the interconnected, porous CNT sponge architecture and improved electronic conductivity between the compressed CNTs. Deterministic 3D electrode architectures can also be directly synthesized via the assembly of two or more materials into a dense structure while retaining interconnected electron and ion transport pathways.[17–20] Sun et al. showed that tuning the graphene pore size in a Nb_2O_5/holey-graphene composite allowed fast energy storage at rates up to 100*C* with active mass loading up to 11 mg cm^{-2}.[17] Furthermore, the use of low density carbons such as graphene or carbon nanotubes is important to achieve electrode architectures with high gravimetric capacity, energy density, and power density.[17,21] Kwon et al. demonstrated the importance of surface functionalization in forming a desired electrode architecture by mixing polyethylene glycol-coated magnetite nanoparticles with few-wall CNTs, carbon particles, and a conjugated polymer.[20] The conjugated polymer served as a linker between the CNTs and magnetite nanoparticles to improve electronic connectivity, and the carbon particles increased the

porosity leading to lower electrode resistance and faster kinetics. Although CNTs fit the criteria for a low density, conductive scaffold component, most existing works rely on a metal substrate to grow aligned CNTs and subsequently deposit an active material or report free-standing electrodes with randomly oriented CNTs that rely on additional components (and thus additional mass) to alter the electrode architectures.[22–25] Based on these successful electrode designs, the critical attributes of a high performance deterministic 3D electrode architecture include: (1) the presence of interconnected networks for electrons and electrolyte ions, (2) uniform distribution of the redox active mass, and (3) good interfacial adhesion between the conductive and active materials.[26–28] However, many challenges remain, including: (1) reducing the areal mass density of the conductive scaffold, (2) retaining high utilization of the TMO at rates > 10*C*, (3) ensuring reproducibility between electrodes and homogeneity within each 3D electrode, and (4) developing scalable fabrication techniques for all the architecture components.[29–32]

Here, we present a scalable route towards a reproducible, homogeneous, and high mass loading deterministic 3D electrode architecture consisting of electrodeposited MoO_3 on a CNT foam scaffold. The low density CNT foam is tunable in thickness and electronically conductive, rendering it an ideal scaffold material. It also features aligned CNTs that are well-connected through the length of the foam without requiring any metal substrate. MoO_3 was selected as a model intercalation-type TMO that can be electrodeposited from aqueous solutions.[33–35] While commercially-relevant cathode materials can be electrodeposited, this requires high temperature molten salt electrolytes that may lead to the corrosion or decomposition of the CNT foam. X-ray micro-computed tomography (micro-CT) shows that the electrodeposited oxide is uniform throughout the volume of the 3D CNT foam scaffold, enabling high reproducibility between electrodes. The 3D architecture enabled good utilization of active material, with near-theoretical specific capacity for Li^+ de/intercalation into MoO_3 for charge/discharge times of ~ 1.7 hours.

Furthermore, an electrode with ~17 mg cm^{-2} of MoO_3 on a 50 layer (50L) CNT foam delivered areal and volumetric capacities of 4.5 mAh cm^{-2} and 290 mAh cm^{-3} and 55% of the capacity was retained at a charge/discharge time of 10 minutes. Overall, this work demonstrates a simple, scalable approach to achieve high areal and volumetric charge storage capacity by electrodepositing a conformal coating of active material on a free-standing, aligned CNT foam with well distributed charge (electron and ion) transport pathways.

2. EXPERIMENTAL SECTION

2.1. Synthesis of CNT foams. Vertically aligned CNT forests were grown on a quartz substrate using iron chloride ($FeCl_2$) as a catalyst and acetylene, argon, and chlorine gases, as described previously.[36,37] The CNTs within the arrays are approximately 1 mm in length and have diameters ranging from 25-40 nm.[38] The vertically aligned CNTs were drawn from the quartz substrate and wound around a stainless steel mandrel. The number of CNT layers was controlled by the number of mandrel rotations. The layered CNT sheets were infiltrated with pyrolytic carbon in a furnace under the flow of acetylene gas while the pressure was maintained at 30 Torr during the deposition time of 2 hours. The pyrolytic carbon coating was used to prevent the CNTs from collapsing onto each other. The coating increases the diameter of the CNTs to approximately 150 nm, increases the surface area,[39,40] and forms permanent interconnections between crossing and bundled CNTs in the CNT foams. This allows the foam to have resiliency while retaining a porosity of 99.7%.[41] The CNT foams used in this study had an ultra low density of 1.78 mg cm^{-3}.

2.2 Synthesis of MoO_3/CNT foam electrodes. In a typical synthesis, a 1 cm × 2 cm piece of CNT foam was plasma cleaned for 3 minutes at low power (Harrick Plasma PDC-32G). The CNT foam was subsequently dried at 60°C for 1 hour to remove surface water for accurate

measurement of the CNT foam mass. Aluminum foil was folded over a small portion of the CNT foam to ensure good electronic contact to the potentiostat during electrodeposition.

Molybdenum oxide hydrates were electrodeposited onto the CNT foam working electrode using cyclic voltammetry in a 50 mL glass three-neck round-bottom flask. The counter electrode was a platinum rod (99.997%, Alfa Aesar) and the reference electrode was Ag/AgCl in 4M KCl (Pine Instruments). The electrodeposition bath consisted of 0.5M $Na_2MoO_4 \cdot 2H_2O$ (Acros) in deionized water, with H_2SO_4 (Fisher Scientific) added until the solution pH reached 2 (measured using a Mettler Toledo FiveEasy pH meter). A potentiostat (BioLogic, MPG2) was used to sweep the potential between -1.2 and 0.4 V vs. Ag/AgCl with a 60 mV s^{-1} sweep rate and two-minute rests at open-circuit voltage between each cycle. Each cycle took ~ 54 seconds to complete. The number of cycles was changed to adjust the deposited mass. A fresh electrodeposition bath was used for each electrodeposition to ensure the same solution initial composition, concentration, and pH. After electrodeposition, the working electrode was removed from the aluminum foil, thoroughly rinsed with deionized water, and placed on a Kimwipe to absorb any excess solution. The composite electrodes were then sandwiched between two pieces of weigh paper and calendered 3 times between stainless steel rollers that were separated by 100 μm (plus the thickness of the two sheets of weigh paper, ~67 μm). The calendered electrodes were dried overnight in a 60°C oven and subsequently calcined in a tube furnace (MTI Corporation GSL-1500X) at 350°C in air for 5 hours using a 4°C/min ramp rate. The electrode mass decreased by ~10 wt% after this heat treatment, which is attributed to the evaporation of residual electrodeposition solution trapped in the pores of the CNT foam. **Table S1** summarizes the geometric area and mass of MoO_3 on each of the electrodes.

2.3 Physical Characterization. Raman spectra were obtained using a WiTEC alpha300R confocal Raman microscope with a laser wavelength of 532 nm and a 100× objective. X-ray diffraction (XRD) was performed on a crystalline electrode using a Rigaku SmartLab X-ray diffractometer in the standard Bragg-Brentano geometry with Cu Kα (λ = 1.542 Å) radiation. Morphology of the electrode was obtained via scanning electron microscopy (SEM; field emission FEI Verios 460L). The 3D architecture of the electrode was characterized with X-ray micro-CT (Zeiss Xradia 510 Versa). ImageJ was used to measure the electrodeposited area and a micrometer caliper (Mitutoyo) was used to measure the electrode thickness.

2.4 Electrochemical Characterization. The electrochemical intercalation reaction of Li^+ into the MoO_3/CNT foam electrode architecture was studied in a 50 mL glass three-electrode cell inside an Ar-filled glovebox with <0.5 ppm of H_2O and O_2. The reference and counter electrodes were Li metal, and the working electrode was an MoO_3/CNT foam electrode. The electrolyte was 1M $LiClO_4$ in propylene carbonate (PC; Sigma Aldrich). A potentiostat (BioLogic, VMP3) was used to perform cyclic voltammetry measurements from 1 to 4 V vs. Li/Li^+ (unless otherwise noted) with sweep rates ranging from 0.5 to 10 mV s^{-1} (while not directly convertible, these timescales correspond to *C* rates from 0.6*C* to 12*C*). Capacities were calculated according to Equation 1 using the cathodic (negative) current of the second cycle for each sweep rate:

$$C = \int i dt \tag{1}$$

The capacity was subsequently normalized by either the mass of MoO_3 (for specific capacity) or the area of the active region (for areal capacity). Electrochemical impedance spectroscopy (EIS) was performed at open circuit voltage with a 10 mV amplitude in the frequency range of 100 mHz to 500 kHz. Galvanostatic charge/discharge cycling was performed between 1 to 4 V

vs. Li/Li^+. The *C*-rate was calculated based on the full theoretical capacity of MoO_3 (280 mAh g^{-1}).

3. RESULTS AND DISCUSSION

Figure 1a schematically summarizes the procedure used to synthesize the three dimensionally architected MoO_3 on CNT foam electrodes. The proposed electrode fabrication process relies on an interconnected, electronically conductive scaffold of CNTs with large pore volume, which limits its application to such materials, and not raw CNT powder. Free-standing CNT foam scaffolds were prepared by drawing vertically-aligned CNTs from an array and winding them around a stainless steel mandrel. The number of rotations of the mandrel controlled the number of CNT layers, and thus the CNT foam thickness. The as-drawn CNT structures were not elastic and could be permanently damaged after compression. Once the desired number of CNT layers was obtained, they were infiltrated with pyrolytic carbon to prevent the layers from collapsing. **Figure S1** shows the scale of the prepared CNT foams, and **Figure S2** shows the alignment and high porosity of the conductive CNT foam scaffolds.

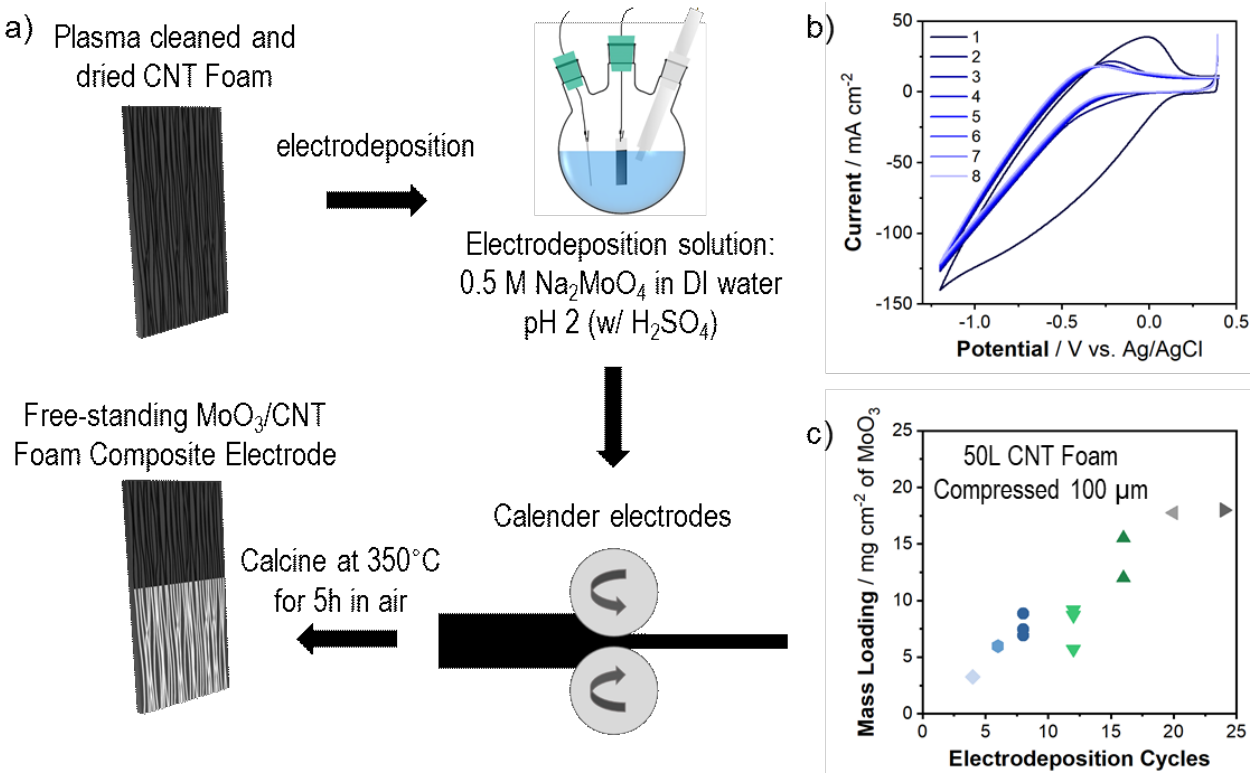

Figure 1. a) Schematic of the fabrication process to obtain 3D MoO_3/CNT foam electrodes. b) Cyclic voltammetry of the electrodeposition process at 60 mV s^{-1} for 8 cycles in an acidic molybdate solution; the reduction current corresponds to the formation of a hydrated molybdenum oxide. c) Nearly linear increase of the areal MoO_3 mass loading on 50 layer CNT foams with the number of electrodeposition cycles. Shapes and colors represent different electrodeposition cycles and each data point represents a different electrode.

The readily-scalable electrodeposition of MoO_3 onto CNT foams was performed from a room temperature acidified aqueous sodium molybdate solution. The pyrolytic carbon coating on the CNTs coupled with the plasma cleaning step in the scaffold preparation results in higher surface area for nucleation of the electrodeposit and sufficient defects for wetting of the aqueous electrolyte within the foam. The presence of defects in the CNT/pyrolytic carbon scaffold was confirmed via Raman spectroscopy (**Figure S3**). The ratio of the D and G band intensities (I_D/I_G),

which represent defect-induced sp^3 and graphitic sp^2 carbon, respectively, is used to quantify the defect concentration in carbon materials.[42] **Figure S3** shows that I_D/I_G increased from 0.71 to 1.25 upon plasma cleaning the scaffold, which resulted in enhanced hydrophilicity. Cyclic voltammetry (shown in **Figure 1b**) was used to electrodeposit molybdenum oxide hydrates onto the free-standing CNT foams. According to McEvoy and Stevenson,[43] electrodeposition from an acidified molybdate solution containing iso-polymolybdate ions proceeds via a series of reduction reactions to yield a hydrated molybdenum oxide with mixed valency. Since this is a faradaic process involving charge transfer from the electrode to the electrodeposited film, it produces a film that is chemically bound, and thus well-adhered, to the substrate (*vide infra*). The electrodeposit was crystallized and oxidized to orthorhombic α-MoO_3 by calcination at 350°C in air for 5 hours.

Raman spectroscopy was used to characterize the local structure of the molybdenum oxide before and after calcination (**Figure 2a**). After electrodeposition and calendering, the Raman spectrum of the electrode was characterized by broad peaks in the region of Raman-active MoO_3 vibrational modes, indicative of an amorphous deposit. The subsequently calcined electrode consisted of α-MoO_3 whose Raman spectrum agrees well with prior reports and the primary peaks are due to different molybdenum-oxygen stretching (ν) modes.[44–46] XRD of the calcined electrode (**Figure 2b**) confirmed that the amorphous as-deposited material transformed to α-MoO_3 upon calcination. We also observed a small amount of a water-soluble impurity phase, whose presence decreased after washing with deionized water (**Figure S4**).

A major benefit of the electrodeposition protocol is excellent control over the oxide mass loading simply by controlling the number of cyclic voltammetry cycles. **Figure 1c** shows that the mass loading of MoO_3 increased nearly linearly with the number of cyclic voltammetry cycles. On a 50 layer CNT foam, the geometric areal MoO_3 mass loading increased from 3.25 mg cm^{-2} to

15.5 mg cm^{-2} when the number of electrodeposition cycles increased from 4 to 16. **Figure S5** shows optical images of the composite electrodes after electrodeposition, calendering, and calcination. The areal MoO_3 loading started to plateau at ~17 mg cm^{-2}, corresponding to 20 electrodeposition cycles, at which point the electrodeposit thickness was so large that the electrodes become very dense (*vide infra*). This suggests that the maximum areal loading is limited by the total surface area of the CNT foam scaffold and the thickness and nature of the oxide deposit, which control electron transport from the CNT scaffold to the electrochemical interface. The self-limiting nature of the electrodeposition process ensured that there would be sufficient electronic conductivity to the surfaces of the MoO_3 to enable charge transfer necessary for electrochemical Li^+ intercalation.

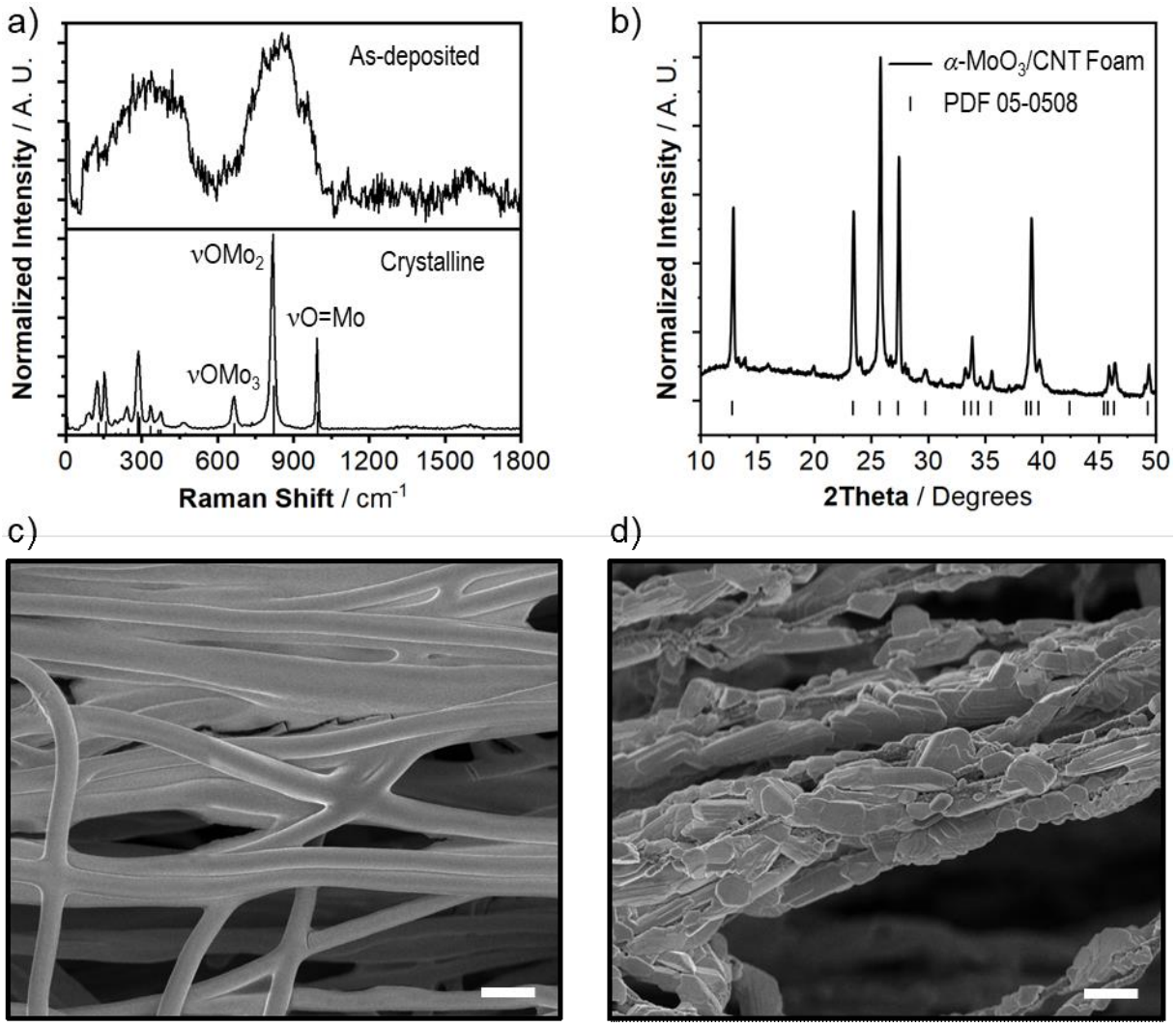

Figure 2. a) Raman spectra of the as-electrodeposited, amorphous molybdenum oxide on CNT foam electrode and the electrode after calcination to yield α-MoO_3. νMo=O, νOMo_2, and νOMo_3 indicate different stretching modes.[46] b) XRD of the calcined electrode confirming the presence of crystalline α-MoO_3 on the CNT foam after calcination. SEM images show c) the smooth and conformal morphology of the as-electrodeposited, amorphous oxide on CNT foam, and d) the formation of well adhered grains of α-MoO_3 on the CNT foam after calcination. Scale bars are 1 μm in c and d.

SEM was used to characterize the morphology of the MoO_3/CNT foam electrodes after electrodeposition, calcination, and as a function of electrodeposition cycle. After electrodeposition (**Figure 2c**), the oxide is conformally coated on the CNTs with a smooth morphology. After calcination (**Figure 2d**) the now-crystalline oxide remained adhered to the CNTs, and the morphology changed from a smooth to a faceted, grain-like coating. **Figure 3a-d** shows that, in agreement with the weight measurements in **Figure 1c**, the thickness of the oxide increased with the number of electrodeposition cycles. The low magnification images in **Figure 3** also show that the porosity decreased as the areal MoO_3 loading increased from 3.25 (4 cycles) to 15.5 mg cm^{-2} (16 cycles). Importantly, micron-scale pores, which allow for electrolyte diffusion into the electrode, were present in all electrodes.

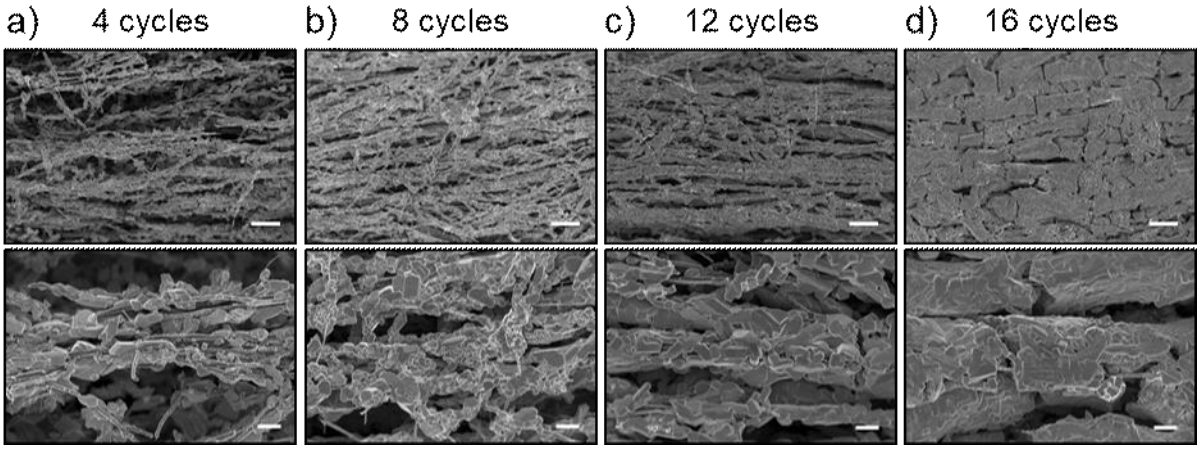

Figure 3. SEM images of the progression of decreased pore size and increased electrodeposit thickness with increasing number of electrodeposition cycles, and thus areal MoO_3 loading, for samples with a) 4 cycles, b) 8 cycles, c) 12 cycles, and d) 16 cycles. Scale bars in the top row are 5 μm and in the bottom row are 1 μm.

X-ray micro-CT allows for characterization of the 3D architecture and is critical to understand the distribution of the active materials within the electrode volume, information that cannot be captured from 2D techniques such as SEM.[47] **Supplemental Movie 1** shows a 3D reconstruction from micro-CT of an 8 cycle electrodeposit on a 20L CNT foam electrode. **Figure 4** shows cross-sectional images taken 25%, 50%, and 75% of the way through the electrode thickness. **Supplemental Movie 1** and the cross-sectional images in **Figure 4** clearly show the uniformity of the MoO_3 electrodeposit, aligned electrode architecture, and interconnected porosity as compared to a cross-section of the pristine CNT foam in **Figure S6**. This data demonstrates that the aligned CNT foams are electronically conductive and that the electrodeposition of the oxide occurs readily throughout the volume. The cross-sectional SEM images in **Figure 5** confirm the uniformity of the electrodeposit through the thickness of non-compressed and compressed MoO_3/CNT foam electrodes. The uniformity is especially evident in the backscattered electron images (bottom images) in **Figure 5**, in which higher atomic weight elements (Mo) are brighter than lower atomic weight elements (C). Electrodes that were not compressed via calendering (**Figure 5a**) contained large micron-size pores that contribute excess porosity for electrolyte permeation, beyond what is necessary for good electrolyte wetting and high ion migration. After calendering (**Figure 5b**), there was a significant decrease in the presence of these large pores, showing that simple compression enables control of electrode porosity which will enable higher volumetric and specific capacity.

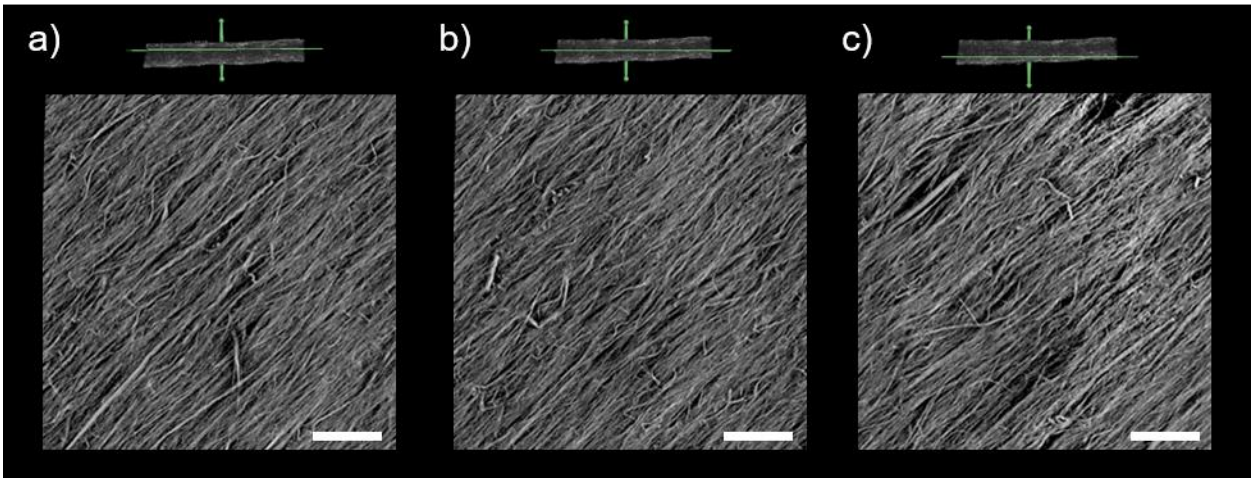

Figure 4. Reconstructed micro-CT cross-sectional images of an 8 cycle electrodeposited MoO_3/CNT foam (20 layer) electrode a) 25%, b) 50% and c) 75% through the thickness of the foam showing the uniformity of the oxide coating and alignment of the CNTs. The horizontal lines in the top images show location of the cross-sectional scan along the electrode thickness. Scale bars are 100 μm.

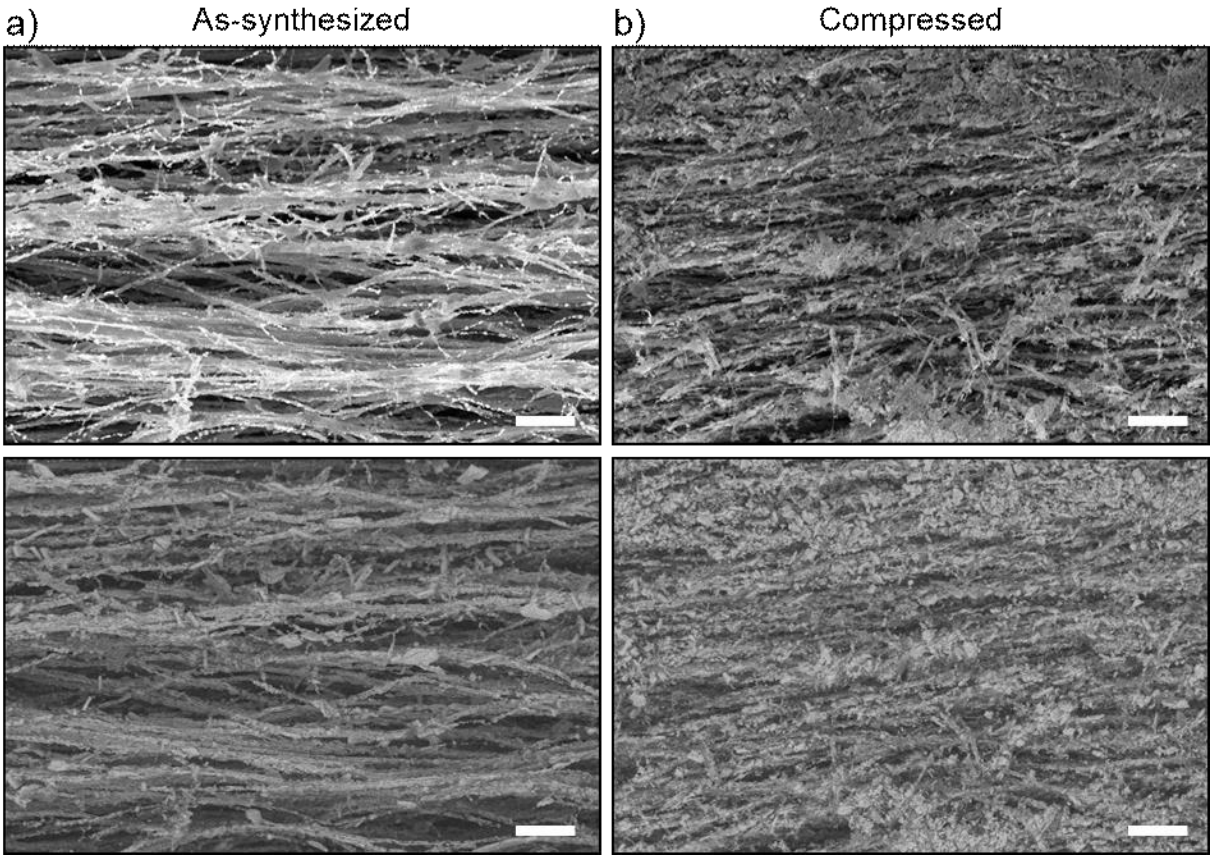

Figure 5. Cross-sectional SEM images of a) an as-synthesized (non-compressed) electrode and b) a compressed electrode. The secondary electron image (top) and back-scattered electron image (bottom) for both electrodes revealed the uniform distribution of MoO_3 throughout the CNT foam thickness and significant reduction in porosity after compression. The scale bars in all images are 5 μm.

The electrochemical energy storage performance of the MoO_3/CNT foam electrode architectures was studied using cyclic voltammetry in a three-electrode cell with Li metal counter and reference electrodes and a 1M $LiClO_4$ in PC electrolyte. The electrochemical intercalation of Li^+ into MoO_3 can be expressed as:

$$MoO_3 + xLi^+ + xe^- \leftrightarrow Li_xMoO_3 \quad (2)$$

Up to 1.5 Li^+ can be intercalated per mole of MoO_3, which corresponds to a theoretical intercalation capacity of 280 mAh g^{-1}. **Figure 6a** shows the evolution of the shape and redox peak positions with increased sweep rate for an electrode with moderate MoO_3 mass loading (7.5 mg cm^{-2}). The electrochemical response of the CNT foam is also shown, and in this potential range contributes only a small amount of current from the charging of the electric double layer. The vast majority of the current, and thus charge storage, in the electrodes comes from electrochemical intercalation and deintercalation of Li^+ into and out of the interlayer of MoO_3, which is characterized by a well-defined set of peaks at ~ 2.12 V (for intercalation) and 2.74 V (for de-intercalation) at 0.5 mV s^{-1}. While the peak voltage separation increased with sweep rate, the de/intercalation peaks remained within the potential window even at 5 mV/s (t = 10 minutes), a timescale that approximately corresponds to a 6C rate.

The rate controlling kinetics of electrochemical ion intercalation in a cyclic voltammetry experiment can be approximated by considering the relationship of the peak current (i_p) with the sweep rate (v):[48]

$$i_p = a v^b \quad (3)$$

Assuming that electrolyte transport is not rate-limiting, two limiting cases exist: a b-value of 0.5, which indicates an intercalation reaction limited by solid state semi-infinite diffusion, and a b-value of 1, which indicates surface or interface control.[49] Intermediate b-values are assigned to either combination of solid-state semi-infinite and surface controlled processes[50,51] or the presence of solid-state finite diffusion.[52] Figure 6b shows the log(i_p) vs. log(v) plot for the 7.5 mg cm^{-2} MoO_3/CNT foam between 0.5 and 10 mV s^{-1} (t = 100 to 5 minutes) whose slope was used to determine a b-value of ~0.6. Given the diffusion coefficient of Li^+ in MoO_3 (~ 10^{-12} cm^2 s^{-1})[53] and a diffusion distance of 1,000 to 500 nm (estimated from the thickness of the MoO_3 deposits in **Figure 3b**), the diffusion time for Li^+ is between 167 and 42 minutes, which is longer than the

timescale of the cyclic voltammetry measurements. This, and the *b*-value of ~0.6, indicate that Li^+ intercalation into the MoO_3/CNT foam electrode architecture is limited by solid state Li^+ diffusion. Therefore, the deterministic 3D architecture provides fast electron transport in the solid and sufficient porosity to enable fast electrolyte diffusion as compared to the rate at which the cations diffuse through MoO_3.

Figure 6c and **Figure S7** show cyclic voltammograms at 0.5 mV s^{-1} for electrodes with different mass loadings prepared by, respectively, either changing the number of electrodeposition cycles on 50 layer CNT foams or the number of CNT foam layers (therefore changing the available electrodeposition surface area). As expected, the areal current increases for electrodes with higher MoO_3 mass loading for both CNT foams with more layers and higher electrodeposition cycles. The increase in areal current density also leads to an increase in the current peak separation, likely caused by increased Ohmic and mass transport polarizations in electrodes with high MoO_3 loading. **Figure S8** shows the cyclic voltammograms for each electrode in **Figure 6c**, and the *b*-value calculated for each electrode can be found in **Figure 6d**. The *b*-value remains ~0.5-0.6 for electrodes with mass loading from 3 to 16 mg cm^{-2}, reaffirming that regardless of the mass loading, the electrochemical reaction is limited by solid-state Li^+ diffusion.

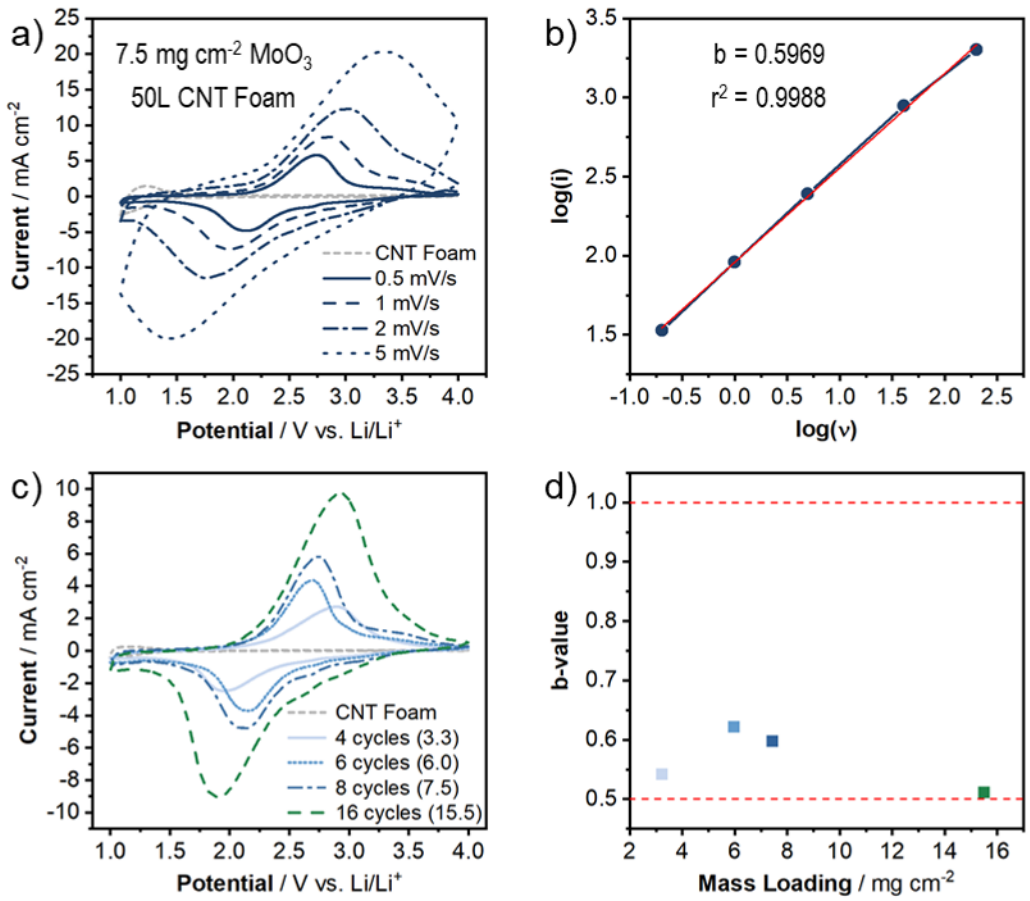

Figure 6. a) Cyclic voltammograms at multiple sweep rates for an 8 cycle, 7.5 mg cm^{-2} MoO_3/CNT foam electrode from 0.5 to 5 mV s^{-1} (t = 100 to 5 minutes). b) Variation of the peak current as a function of sweep rate used to determine the *b*-value. c) Cyclic voltammograms at 0.5 mV s^{-1} and d) variation of the *b*-value as a function of MoO_3 mass loading on MoO_3/CNT foam (50 layer) electrodes.

We calculated the characteristic time associated with charging and discharging,[54] τ, for each electrode by fitting the specific capacity vs. rate data shown in **Figure 7a** to the following equation:

$$\frac{Q}{M} = Q_M\,[1 - (R\tau)^n(1 - e^{-(R\tau)^{-n}})] \qquad (4)$$

Here, $\frac{Q}{M}$ is the measured specific capacity at a given rate R, Q_M is the electrode's maximum achievable capacity at a slow rate, and n is a constant parameter indicative of the rate limiting mechanism. **Figure S9** provides an example of how τ was determined for an 8 cycle (7.5 mg cm^{-2}) electrode. Using this analysis, we find that τ increases as mass loading increases, from 0.39 hours for a 6.0 mg cm^{-2} electrode, to 3.18 hours for a 15.5 mg cm^{-2} electrode (**Figure 7b**.) This analysis indicates that solid-state diffusion becomes rate-limiting with increasing MoO_3 mass loading, in agreement with the cyclic voltammetry peak current analysis.

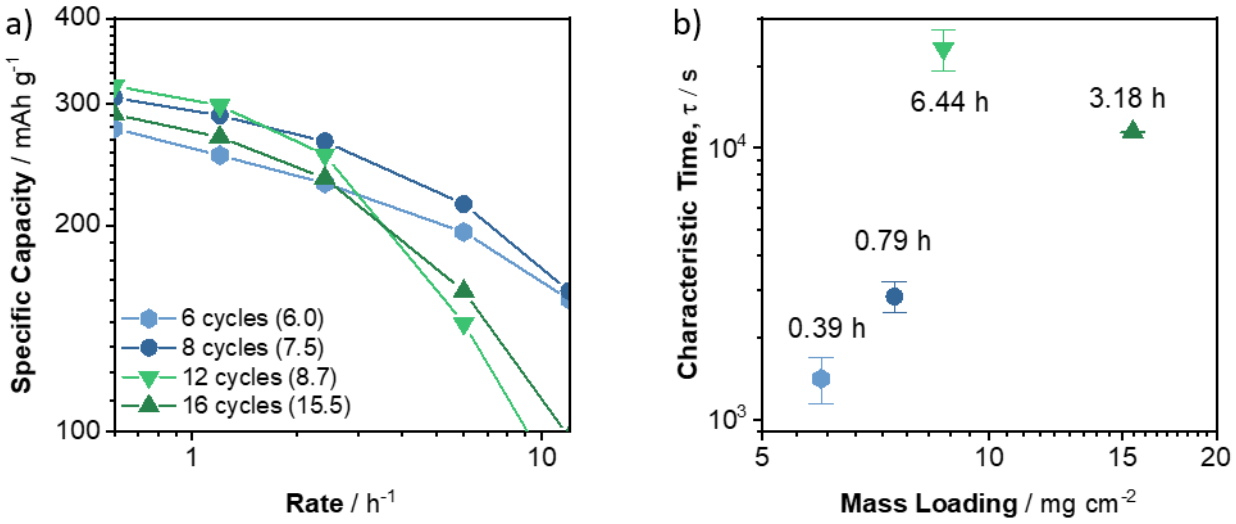

Figure 7. a) Specific capacity vs. rate for different mass loading electrodes. b) The characteristic time (τ) for each electrode determined from Equation 4. The error bars indicate standard error from fitting Equation 4 to the experimental data.

EIS of the electrodes shown in **Figure 6c** was performed at open circuit voltage. **Figure S10** shows the Nyquist plots of each electrode, with the high frequency region shown in more detail in the inset. The 6.0, 7.5, and 15.5 mg cm^{-2} electrodes show similar impedance responses, with a semi-circle in the high frequency region and a slanted line in the low frequency region. These

features are typically ascribed to the charge transfer resistance and diffusion in the electrode, respectively.[55] The higher impedance of the 3.3 mg cm^{-2} electrode is consistent with the higher overpotential observed for this electrode in **Figure 6c**. We hypothesize that this could be related to the microstructure of the 4 cycle deposit, which (unlike the higher mass loadings) does not coat the entire surface of the CNTs.

The electrode performance can be characterized by considering the rate capability of the capacity from both a volumetric and gravimetric standpoint. **Figure 8** compares the normalized capacity, areal capacity, and volumetric capacity as a function of sweep rate for electrodes with MoO_3 mass loading ranging from 3.3 to 15.5 mg cm^{-2}. The rate capability of the normalized capacity enables comparison to the underlying kinetics of the bare CNT foam conductive scaffold. Upon increasing the sweep rate from 0.5 mV s^{-1} to 10 mV s^{-1}, the CNT foam shows a capacity fade of ~ 50%, which is +/- 20% of the capacity fade of the foams with electrodeposited MoO_3. The weight % of CNTs in the electrode architecture was 37% for the 3.3 mg cm^{-2} MoO_3 and decreased as the MoO_3 loading increased, reaching just 13.7% in the 15.5 mg cm^{-2} MoO_3 electrode. The normalized capacity graphs show that even as the weight fraction of the CNTs decreased, the electrodes maintained high rate capability and active material utilization. This result emphasizes that the efficient electronic wiring provided by the aligned CNTs is present throughout the deterministic electrode architecture at all MoO_3 mass loadings. Moreover, the light weight of the CNT foams means that the architectures exhibit high capacities based on the total electrode mass, reaching average values of 200 mAh g^{-1} (**Figure S11**). The decrease in rate capability of electrodes with mass loadings greater than ~ 7.5 mg cm^{-2} can be attributed to the apparent increase in film coverage density on the CNTs (**Figure 3**), resulting in lower electrochemically active surface area and thus fewer active surface sites for electrochemical ion insertion. **Figure 8b,c** show the areal and volumetric capacity as a function of sweep rate and

MoO_3 mass loading. Control over the active material mass loading via electrodeposition as well as high utilization of the MoO_3 allow for high tunability of the final areal and volumetric capacity. This is critically important for electrode architectures, because it demonstrates both scalability and reproducibility of the trends in electrochemical performance at various mass loadings. The trends between number of electrodeposition cycles, mass loading, and areal and volumetric capacities persist despite small scaffold-to-scaffold variations in CNT density (and therefore surface area available for oxide electrodeposition) that may influence the electrodeposited mass loading. The highest areal capacity, 4.5 mAh cm^{-2}, was obtained with a MoO_3 mass loading of 15.5 mg cm^{-2}, which corresponds to a volumetric capacity of 290 mAh cm^{-3}. Importantly, even as the areal capacity increased, the specific capacity remained close to the theoretical capacity indicating excellent utilization of the full thickness of the active material at 0.5 mV s^{-1}. At 5 mV s^{-1}, the highest mass loading electrode still reached an areal capacity of 2.5 mAh cm^{-2}. The capacity retention between these rates demonstrates the deterministic 3D electrodes' ability to provide good electron and ion transport through the aligned fibers in the CNT foam.

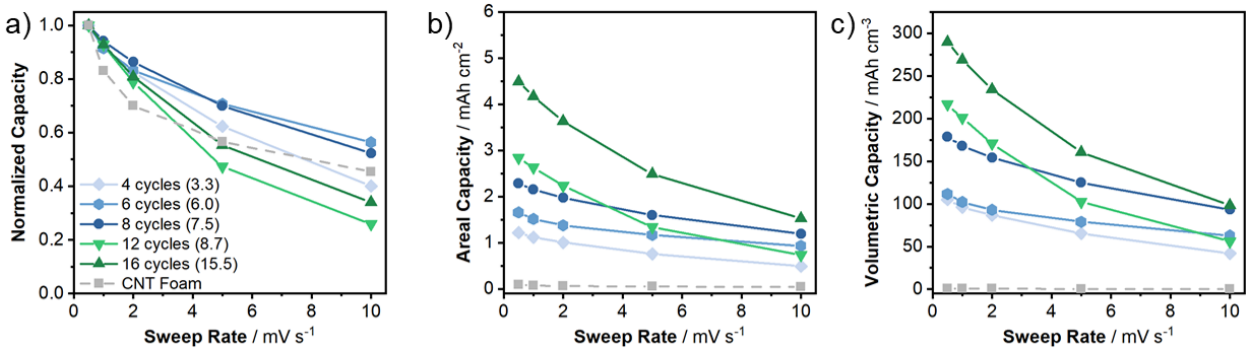

Figure 8. Rate capability for the a) normalized capacity, b) areal capacity, and c) volumetric capacity for different MoO_3 mass loadings on 50L CNT foams. Numbers in parentheses correspond to the mass loading of MoO_3 on the electrode.

Ex situ XRD and Raman spectroscopy after electrochemical cycling at different rates reveal that Li^+ intercalation leads to disorder of the α-MoO_3 structure. The XRD pattern of a cycled electrode (**Figure S12a**) consists of broad peaks in the region of highest intensity peaks of α-MoO_3 and is representative of amorphous MoO_3. The sharp XRD peaks are from absorbed electrolyte salt ($LiClO_4$) that remained in the electrode even after rinsing with dimethyl carbonate. **Figure S12b** shows the Raman spectrum of a cycled electrode. The broad peaks in the region of Raman-active α-MoO_3 vibrational modes are in-line with the XRD results of a more disordered oxide after electrochemical cycling. This structural change is consistent with prior reports that the material undergoes an irreversible transformation in the first few electrochemical cycles.[56–58] The transition from a crystalline to disordered structure does not affect the microstructure or electrode integrity, as observed from *ex situ* SEM (**Figure S13**) after ~ 200 cyclic voltammetry cycles. This indicates that the MoO_3 is well-adhered to the CNT scaffold during electrochemical cycling. Therefore, the capacity decay is attributed as intrinsic to the MoO_3, and not the microstructure or electrode architecture.

Galvanostatic cycling is another popular electrochemical technique for characterizing energy storage materials. The results are complementary to those shown from cyclic voltammetry. **Figure 9a** shows the first three cycles at 0.5*C* (1.3 mA cm^{-2}) for an electrode with a MoO_3 mass loading of 9.3 mg cm^{-2}. The discharge capacity at this rate was 279.4 mAh g^{-1} (2.6 mAh cm^{-2}), essentially the theoretical value for full lithiation of MoO_3. Comparison of the charge/discharge profiles at 0.5*C*, 1*C*, 2*C*, and 5*C* is shown in **Figure 9b** and shows increasing hysteresis between the de/lithiation plateaus and decreasing capacity as the rate increases. The capacity and stability for 5 cycles at each rate is shown in **Figure 9c** and shows that the electrode architecture does allow for high rate capability of a high mass loading oxide electrode. The electrode architecture

exhibited ~60% capacity retention upon increasing the rate from 0.5*C* (*t* = 120 min discharge) to 5*C* (*t* = 12 min discharge). Finally, the electrode was cycled 1,000 times at 5*C* between 1-4 V vs. Li/Li^+ (**Figure S14**). As was observed from cyclic voltammetry, the intrinsic instability of MoO_3[57–59] led to a poor capacity retention of ~44% (67.2 mAh g^{-1}) after 1,000 cycles. For long term cycling, further work is necessary to either stabilize the MoO_3 crystal structure, which has been the topic of recent investigation,[34,57,60–64] or determine an aqueous electrodeposition route for an oxide material that does not undergo such significant structural change.

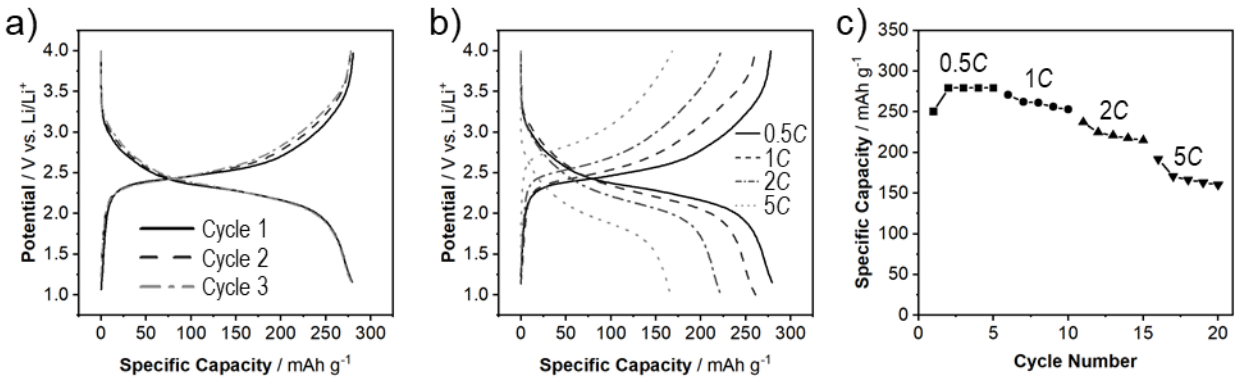

Figure 9. Galvanostatic charge/discharge of a 12 cycle, 9.3 mg cm^{-2} MoO_3/CNT foam electrode for (a) the first 3 cycles at 0.5*C*, (b) at multiple rates between 0.5*C* and 5*C*, and c) capacity retention at each rate for 5 cycles.

Figure 10a,b show a linear increase of the areal and volumetric capacity as a function of MoO_3 mass loading at 0.5 mV s^{-1}. This trend is enabled by the full utilization of the electrodeposited MoO_3 at all mass loadings. The aligned CNTs in the electrode provided continuous electron transport pathways throughout the electrode, and the electrodeposition protocol used for the synthesis of the active material inherently necessitated good electronic contact between the deposited material and the electronically conductive scaffold, which enabled full utilization of the

active material as shown in **Figure 10c**. Values higher than the theoretical capacity, especially for the 4 cycle electrode, could indicate the presence of reversible redox from soluble species (**Figure S4**) although this influence is not clear from the cyclic voltammograms (**Figure S7b**). Furthermore, the efficient packing of the CNTs in the foam led to high volumetric capacity, while maintaining interconnected porosity for diffusion of the electrolyte and complete wetting of the active material. **Figure 10d** shows that the areal capacity of the deterministic MoO_3/CNT foam electrode architecture in this work was higher as compared to commercially-prepared slurry electrodes, several other intercalation-type transition metal oxide electrode architectures, and other MoO_3/CNT electrode architectures (inset) as a function of active material loading.[11,14,17,23,65–70] This demonstrates that the deterministic electrode architecture presented here provides a scalable and reproducible pathway for high mass loading, 3D electrode architectures.

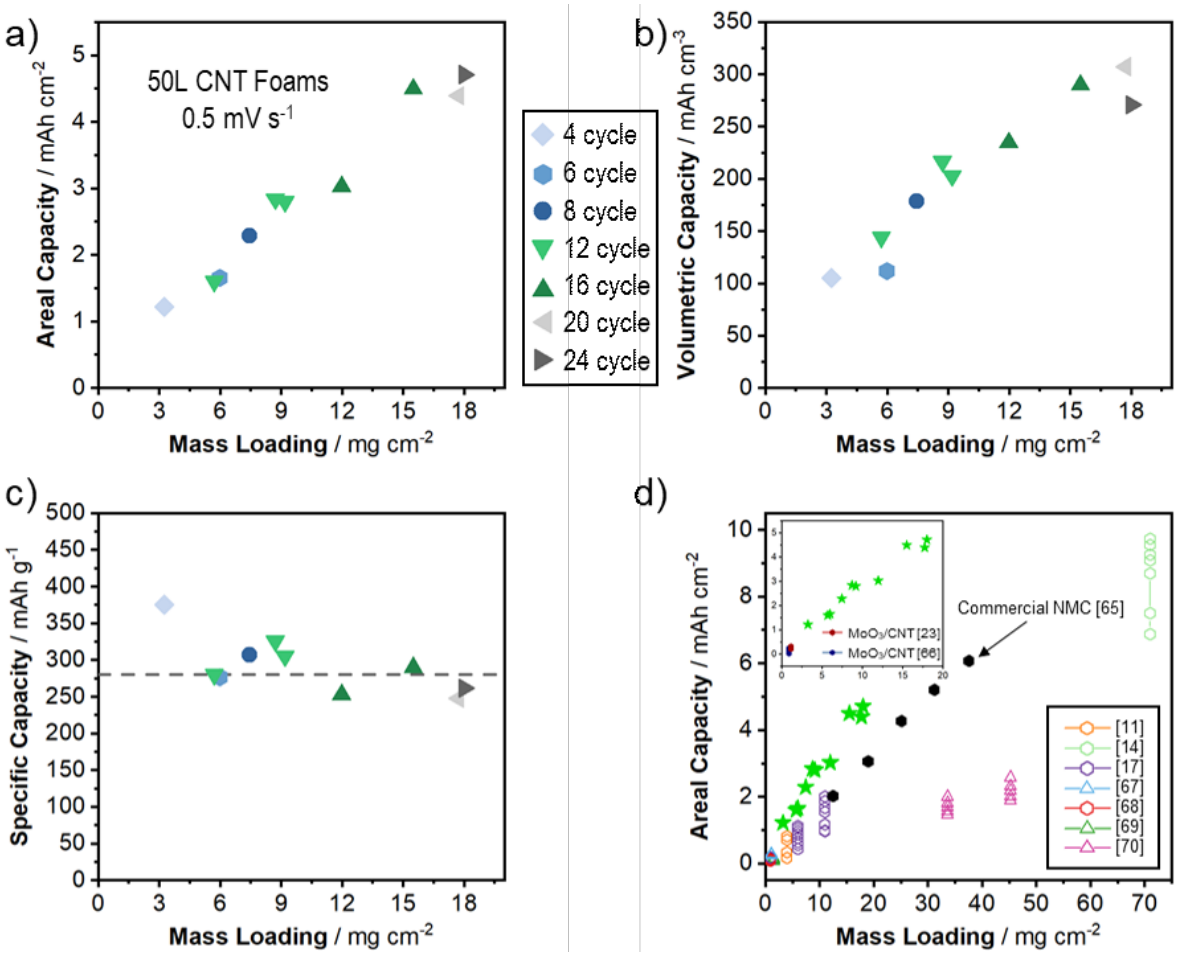

Figure 10. The MoO_3/CNT foam electrode architecture enabled simple tunability of the a) areal capacity and b) volumetric capacity at 0.5 mV s^{-1}. c) The specific capacity was near-theoretical (dashed line; 280 mAh g^{-1}) across a range of MoO_3 mass loadings. d) The electrodes in this work (green stars) trended toward higher areal capacities at lower active material loadings compared to commercial electrodes and other recently reported intercalation-type free standing electrode architectures. Shapes indicate the type of electrolyte solvent used in each study, with hexagons for non-aqueous and triangles for aqueous.

4. CONCLUSIONS

Here, we demonstrate a scalable and reproducible route towards high areal and volumetric capacity deterministic 3D electrode architectures using a tunable CNT foam conductive scaffold and conformal electrodeposition of an intercalation-type transition metal oxide, MoO_3. The number of electrodeposition cycles or CNT foam layers was used to control the amount of MoO_3 deposited on the CNT foams. Electrodeposition ensured good adhesion and electronic contact between the conductive substrate and the active material as well as excellent control over the oxide mass loading as demonstrated by cross-sectional SEM and micro-CT. Furthermore, the CNT foam enabled areal loadings of MoO_3 up to ~17 mg cm^{-2} while maintaining enough porosity for electrolyte to permeate through the entire thickness of the electrode. We found that at 0.5 mV s^{-1} the electrodes delivered near-theoretical specific capacities for Li^+ intercalation into MoO_3 at all mass loadings, which enabled tunable areal and volumetric energy storage performance. The MoO_3/CNT foam electrode architecture with 15.5 mg cm^{-2} of MoO_3 reached areal and volumetric capacities of 4.5 mAh cm^{-2} and 289.7 mAh cm^{-3}, respectively, at 0.5 mV s^{-1} and ~55% of the capacity was retained at 5 mV s^{-1}. This work demonstrated that CNT foam electrodes are good scaffolds for 3D electrode architectures because they are free-standing, electronically conductive, and have high surface area and porosity. After electrodeposition of the active material to achieve conformal deposits on the CNT fibers, the CNTs provided aligned electron transport paths throughout the thick electrodes and the porosity allowed electrolyte to effectively wet all the active material. As a result, the TMO/CNT foam electrode architecture enables high gravimetric utilization of the active material at practical charge/discharge rates, thus enabling tunable areal and volumetric charge storage performance. Future work will focus on increasing the energy storage performance even further, by fabricating CNT foams with higher thickness and surface area for oxide electrodeposition and adapting the manufacturing technique for the deposition of more complex oxide compositions, such as lithiated transition metal oxides used as cathodes in

Li-ion batteries. The results presented here provide a scalable and reproducible pathway towards the development of deterministic, 3D electrode architectures that combine electrodeposition of oxides with CNT foams.

ASSOCIATED CONTENT

Supporting Information.

The Supporting Information to this article is available free of charge.

Digital images of full size CNT foams; SEM images of bare CNT foam; Raman of the CNT foam before and after plasma cleaning; XRD of electrodes after calcination and washing; digital images of MoO_3/CNT foam electrodes; X-ray-CT cross-sectional image of CNT foam; CVs of composite electrodes with different number of CNT layers; CVs of each electrode from Figure 6c from 0.5 to 5 mV s^{-1}; EIS spectra of the electrodes in Figure 6c; Specific capacity based on mass of the electrode as a function of MoO_3 loading; Ex-situ XRD and Raman after electrochemical cycling; CV cycling capacity results and SEM image after cycling for a 7.5 mg cm^{-2} MoO_3/CNT foam electrode; Galvanostatic cycling capacity for a 9.3 mg cm^{-2} MoO_3/CNT foam electrode. (PDF)

Data Availability

The raw and processed data required to reproduce these findings are available to download from Mendeley Data.

AUTHOR INFORMATION

Corresponding Author

Veronica Augustyn – Department of Materials Science and Engineering, North Carolina State University, Raleigh, NC 27606, United States; orcid.org/0000-0001-9885-2882; Email: vaugust@ncsu.edu

Authors

Michael A. Spencer – Department of Materials Science and Engineering, North Carolina State University, Raleigh, NC 27606, United States; orcid.org/0000-0002-9552-2842

Ozkan Yildiz – Department of Textile Engineering, Chemistry, and Science, North Carolina State University, Raleigh, NC 27695

Ishita Kamboj – Department of Materials Science and Engineering, North Carolina State University, Raleigh, NC 27606, United States; orcid.org/0000-0003-0148-0379

Philip D. Bradford – Department of Textile Engineering, Chemistry, and Science, North Carolina State University, Raleigh, NC 27695, United States; orcid.org/0000-0002-4448-5033

Complete contact information is available online.

ACKNOWLEDGEMENTS

This material is based upon work supported by the National Science Foundation under Grant No. CMMI - 1901906. This work was performed in part at the Analytical Instrumentation Facility (AIF) at North Carolina State University, which is supported by the State of North Carolina and the National Science Foundation (award number ECCS-1542015). The AIF is a member of the North Carolina Research Triangle Nanotechnology Network (RTNN), a site in the National Nanotechnology Coordinated Infrastructure (NNCI).

REFERENCES

(1) Thackeray, M. M.; David, W. I. F.; Bruce, P. G.; Goodenough, J. B. Lithium Insertion into Manganese Spinels. *Mater. Res. Bull.* **1983**, *18* (4), 461–472. https://doi.org/10.1016/0025-

5408(83)90138-1.

(2) Mizushima, K.; Jones, P. C.; Wiseman, P. J.; Goodenough, J. B. Li_xCoO_2 ($0 < x < 1$): A New Cathode Material for Batteries of High Energy Density. *Mater. Res. Bull.* **1980**, *15*, 783–789. https://doi.org/10.1016/0167-2738(81)90077-1.

(3) Braun, P. V.; Cho, J.; Pikul, J. H.; King, W. P.; Zhang, H. High Power Rechargeable Batteries. *Curr. Opin. Solid State Mater. Sci.* **2012**, *16* (4), 186–198. https://doi.org/10.1016/j.cossms.2012.05.002.

(4) Augustyn, V.; Simon, P.; Dunn, B. Pseudocapacitive Oxide Materials for High-Rate Electrochemical Energy Storage. *Energy Environ. Sci.* **2014**, *7* (5), 1597. https://doi.org/10.1039/c3ee44164d.

(5) Park, M.; Zhang, X.; Chung, M.; Less, G. B.; Sastry, A. M. A Review of Conduction Phenomena in Li-Ion Batteries. *J. Power Sources* **2010**, *195* (24), 7904–7929. https://doi.org/10.1016/j.jpowsour.2010.06.060.

(6) Kraytsberg, A.; Ein-Eli, Y. Conveying Advanced Li-Ion Battery Materials into Practice The Impact of Electrode Slurry Preparation Skills. *Adv. Energy Mater.* **2016**, *6* (21), 1600655. https://doi.org/10.1002/aenm.201600655.

(7) Ni, J.; Li, L. Cathode Architectures for Rechargeable Ion Batteries: Progress and Perspectives. *Adv. Mater.* **2020**, *32* (28), 1–7. https://doi.org/10.1002/adma.202000288.

(8) Braun, P. V.; Cook, J. B. Deterministic Design of Chemistry and Mesostructure in Li-Ion Battery Electrodes. *ACS Nano* **2018**, *12* (4), 3060–3064. https://doi.org/10.1021/acsnano.8b01885.

(9) Long, J. W.; Rolison, D. R. Architectural Design, Interior Decoration, and Three-Dimensional Plumbing En Route to Multifunctional Nanoarchitectures. *Acc. Chem. Res.* **2007**, *40* (9), 854–862. https://doi.org/10.1021/ar6000445.

(10) Liu, J.; Zheng, Q.; Goodman, M. D.; Zhu, H.; Kim, J.; Krueger, N. A.; Ning, H.; Huang, X.; Liu, J.; Terrones, M.; et al. Graphene Sandwiched Mesostructured Li-Ion Battery Electrodes. *Adv. Mater.* **2016**, *28* (35), 7696–7702. https://doi.org/10.1002/adma.201600829.

(11) Chen, X.; Zhu, H.; Chen, Y.-C.; Shang, Y.; Cao, A.; Hu, L.; Rubloff, G. W. MWCNT/V_2O_5 Core/Shell Sponge for High Areal Capacity and Power Density Li-Ion Cathodes. *ACS Nano* **2012**, *6* (9), 7948–7955. https://doi.org/10.1021/nn302417x.

(12) Dörr, T. S.; Fleischmann, S.; Zeiger, M.; Grobelsek, I.; de Oliveira, P. W.; Presser, V. Ordered Mesoporous Titania/Carbon Hybrid Monoliths for Lithium-Ion Battery Anodes with High Areal and Volumetric Capacity. *Chem. - A Eur. J.* **2018**, *24* (24), 6358–6363. https://doi.org/10.1002/chem.201801099.

(13) Zhang, X.; Ju, Z.; Housel, L. M.; Wang, L.; Zhu, Y.; Singh, G.; Sadique, N.; Takeuchi, K. J.; Takeuchi, E. S.; Marschilok, A. C.; et al. Promoting Transport Kinetics in Li-Ion Battery with Aligned Porous Electrode Architectures. *Nano Lett.* **2019**, *19*, 8255–8261. https://doi.org/10.1021/acs.nanolett.9b03824.

(14) Zheng, J.; Zhao, Q.; Liu, X.; Tang, T.; Bock, D. C.; Bruck, A. M.; Tallman, K. R.; Housel, L. M.; Kiss, A. M.; Marschilok, A. C.; et al. Nonplanar Electrode Architectures for Ultrahigh Areal Capacity Batteries. *ACS Energy Lett.* **2019**, *4* (1), 271–275. https://doi.org/10.1021/acsenergylett.8b02131.

(15) Zhang, H.; Ning, H.; Busbee, J.; Shen, Z.; Kiggins, C.; Hua, Y.; Eaves, J.; Davis, J.; Shi, T.; Shao, Y.-T.; et al. Electroplating Lithium Transition Metal Oxides. *Sci. Adv.* **2017**, *3* (5), e1602427. https://doi.org/10.1126/sciadv.1602427.

(16) Chen, Y.; Wang, Y.; Wang, Z.; Zou, M.; Zhang, H.; Zhao, W.; Yousaf, M.; Yang, L.; Cao, A.; Han, R. P. S. Densification by Compaction as an Effective Low-Cost Method to Attain a High Areal Lithium Storage Capacity in a CNT@Co_3O_4 Sponge. *Adv. Energy Mater.* **2018**, *8* (19), 1702981. https://doi.org/10.1002/aenm.201702981.

(17) Sun, H.; Mei, L.; Liang, J.; Zhao, Z.; Lee, C.; Fei, H.; Ding, M.; Lau, J.; Li, M.; Wang, C.; et al. Three-Dimensional Holey-Graphene/Niobia Composite Architectures for Ultrahigh-Rate Energy Storage. *Science* **2017**, *356* (6338), 599–604. https://doi.org/10.1126/science.aam5852.

(18) Zhang, H.; Braun, P. V. Three-Dimensional Metal Scaffold Supported Bicontinuous Silicon

Battery Anodes. *Nano Lett.* **2012**, *12* (6), 2778–2783. https://doi.org/10.1021/nl204551m.

(19) Zhang, H.; Yu, X.; Braun, P. V. Three-Dimensional Bicontinuous Ultrafast-Charge and-Discharge Bulk Battery Electrodes. *Nat. Nanotechnol.* **2011**, *6* (5), 277–281. https://doi.org/10.1038/nnano.2011.38.

(20) Kwon, Y.-H. H.; Park, J. J.; Housel, L. M.; Minnici, K.; Zhang, G.; Lee, S. R.; Lee, S. W.; Chen, Z.; Noda, S.; Takeuchi, E. S.; et al. Carbon Nanotube Web with Carboxylated Polythiophene 'Assist' for High-Performance Battery Electrodes. *ACS Nano* **2018**, acsnano.7b08918. https://doi.org/10.1021/acsnano.7b08918.

(21) Gogotsi, Y.; Simon, P. True Performance Metrics in Electrochemical Energy Storage. *Science* **2011**, *334*, 917–918. https://doi.org/10.1126/science.1213003.

(22) Evanoff, K.; Khan, J.; Balandin, A. A.; Magasinski, A.; Ready, W. J.; Fuller, T. F.; Yushin, G. Towards Ultrathick Battery Electrodes: Aligned Carbon Nanotube-Enabled Architecture. *Adv. Mater.* **2012**, *24* (4), 533–537. https://doi.org/10.1002/adma.201103044.

(23) Zhang, H.; Liu, X.; Wang, R.; Mi, R.; Li, S.; Cui, Y.; Deng, Y.; Mei, J.; Liu, H. Coating of α-MoO_3 on Nitrogen-Doped Carbon Nanotubes by Electrodeposition as a High-Performance Cathode Material for Lithium-Ion Batteries. *J. Power Sources* **2015**, *274*, 1063–1069. https://doi.org/10.1016/j.jpowsour.2014.10.136.

(24) Lee, S. Y.; Cho, S. J.; Choi, K. H.; Yoo, J. T.; Kim, J. H.; Lee, Y. H.; Chun, S. J.; Park, S. B.; Choi, D. H.; Wu, Q.; et al. Hetero-Nanonet Rechargeable Paper Batteries: Toward Ultrahigh Energy Density and Origami Foldability. *Adv. Funct. Mater.* **2015**, *25* (38), 6029–6040. https://doi.org/10.1002/adfm.201502833.

(25) Ban, C.; Wu, Z.; Gillaspie, D. T.; Chen, L.; Yan, F.; Blackburn, J. L.; Dillon, A. C. Nanostructured Fe_3O_4/SWNT Electrode: Binder-Free and High-Rate Li-Ion Anode. *Adv. Mater.* **2010**, *22* (20), 145–149. https://doi.org/10.1002/adma.200904285.

(26) Zhang, X.; Ju, Z.; Zhu, Y.; Takeuchi, K. J.; Takeuchi, E. S.; Marschilok, A. C.; Yu, G. Multiscale Understanding and Architecture Design of High Energy/Power Lithium-Ion Battery Electrodes.

Adv. Energy Mater. **2021**, *11* (2). https://doi.org/10.1002/aenm.202000808.

(27) Wei, T. S.; Ahn, B. Y.; Grotto, J.; Lewis, J. A. 3D Printing of Customized Li-Ion Batteries with Thick Electrodes. *Adv. Mater.* **2018**, *30* (16), 1–7. https://doi.org/10.1002/adma.201703027.

(28) Sander, J. S.; Erb, R. M.; Li, L.; Gurijala, A.; Chiang, Y. M. High-Performance Battery Electrodes via Magnetic Templating. *Nat. Energy* **2016**, *1* (8), 1–7. https://doi.org/10.1038/nenergy.2016.99.

(29) Spencer, M. A.; Augustyn, V. Free-Standing Transition Metal Oxide Electrode Architectures for Electrochemical Energy Storage. *J. Mater. Sci.* **2019**, *54* (20), 13045–13069. https://doi.org/10.1007/s10853-019-03823-y.

(30) Sun, H.; Zhu, J.; Baumann, D.; Peng, L.; Xu, Y.; Shakir, I.; Huang, Y.; Duan, X. Hierarchical 3D Electrodes for Electrochemical Energy Storage. *Nat. Rev. Mater.* **2019**, *4* (1), 45–60. https://doi.org/10.1038/s41578-018-0069-9.

(31) Crabtree, G.; Rubloff, G.; Takeuchi, E. *Basic Research Needs for Next Generation Electrical Energy Storage*; Washington, DC, 2017.

(32) Liu, Y.; Zhu, Y.; Cui, Y. Challenges and Opportunities towards Fast-Charging Battery Materials. *Nat. Energy* **2019**, *4* (7), 540–550. https://doi.org/10.1038/s41560-019-0405-3.

(33) Besenhard, J. O.; Schöllhorn, R. The Discharge Reaction Mechanism of the MoO_3 Electrode in Organic Electrolytes. *J. Power Sources* **1976**, *1* (3), 267–276. https://doi.org/10.1016/0378-7753(76)81004-X.

(34) de Castro, I. A.; Datta, R. S.; Ou, J. Z.; Castellanos-Gomez, A.; Sriram, S.; Daeneke, T.; Kalantar-zadeh, K. Molybdenum Oxides – From Fundamentals to Functionality. *Adv. Mater.* **2017**, *29* (40). https://doi.org/10.1002/adma.201701619.

(35) Hu, X.; Zhang, W.; Liu, X.; Mei, Y.; Huang, Y. Nanostructured Mo-Based Electrode Materials for Electrochemical Energy Storage. *Chem. Soc. Rev.* **2015**, *44* (8), 2376–2404. https://doi.org/10.1039/c4cs00350k.

(36) Fu, K.; Yildiz, O.; Bhanushali, H.; Wang, Y.; Stano, K.; Xue, L.; Zhang, X.; Bradford, P. D. Aligned Carbon Nanotube-Silicon Sheets: A Novel Nano-Architecture for Flexible Lithium Ion

Battery Electrodes. *Adv. Mater.* **2013**, *25* (36), 5109–5114. https://doi.org/10.1002/adma.201301920.

(37) Faraji, S.; Yildiz, O.; Rost, C.; Stano, K.; Farahbakhsh, N.; Zhu, Y.; Bradford, P. D. Radial Growth of Multi-Walled Carbon Nanotubes in Aligned Sheets through Cyclic Carbon Deposition and Graphitization. *Carbon N. Y.* **2017**, *111*, 411–418. https://doi.org/https://doi.org/10.1016/j.carbon.2016.10.012.

(38) Yildiz, O.; Bradford, P. D. Aligned Carbon Nanotube Sheet High Efficiency Particulate Air Filters. *Carbon N. Y.* **2013**, *64*, 295–304. https://doi.org/https://doi.org/10.1016/j.carbon.2013.07.066.

(39) Bradford, P. D.; Wang, X.; Zhao, H.; Zhu, Y. T. Tuning the Compressive Mechanical Properties of Carbon Nanotube Foam. *Carbon N. Y.* **2011**, *49* (8), 2834–2841. https://doi.org/https://doi.org/10.1016/j.carbon.2011.03.012.

(40) Liu, Y.; Ba, H.; Nguyen, D.-L.; Ersen, O.; Romero, T.; Zafeiratos, S.; Begin, D.; Janowska, I.; Pham-Huu, C. Synthesis of Porous Carbon Nanotubes Foam Composites with a High Accessible Surface Area and Tunable Porosity. *J. Mater. Chem. A* **2013**, *1* (33), 9508. https://doi.org/10.1039/c3ta10695k.

(41) Faraji, S.; L. Stano, K.; Yildiz, O.; Li, A.; Zhu, Y.; Bradford, P. D. Ultralight Anisotropic Foams from Layered Aligned Carbon Nanotube Sheets. *Nanoscale* **2015**, *7* (40), 17038–17047. https://doi.org/10.1039/C5NR03899E.

(42) Pimenta, M. A.; Dresselhaus, G.; Dresselhaus, M. S.; Canc, L. G. Studying Disorder in Graphite-Based Systems by Raman Spectroscopy W. **2007**, 1276–1291. https://doi.org/10.1039/b613962k.

(43) McEvoy, T. M.; Stevenson, K. J. Elucidation of the Electrodeposition Mechanism of Molybdenum Oxide from Iso- and Peroxo-Polymolybdate Solutions. *J. Mater. Res.* **2004**, *19* (2), 429–438. https://doi.org/10.1557/jmr.2004.19.2.429.

(44) Dieterle, M.; Weinberg, G.; Mestl, G. Raman Spectroscopy of Molybdenum Oxides. *Phys. Chem. Chem. Phys.* **2002**, *4* (5), 812–821. https://doi.org/10.1039/b107012f.

(45) Haro-Poniatowski, E.; Julien, C.; Pecquenard, B.; Livage, J.; Camacho-López, M. A. Laser-

Induced Structural Transformations in MoO_3 Investigated by Raman Spectroscopy. *J. Mater. Res.* **1998**, *13* (4), 1033–1037. https://doi.org/10.1557/JMR.1998.0144.

(46) Seguin, L.; Figlarz, M.; Cavagnat, R.; Lassègues, J.-C. Infrared and Raman Spectra of MoO_3 Molybdenum Trioxides and $MoO_3 \cdot XH_2O$ Molybdenum Trioxide Hydrates. *Spectrochim. Acta Part A* **1995**, *51* (8), 1323–1344. https://doi.org/10.1016/0584-8539(94)00247-9.

(47) Lu, X.; Bertei, A.; Finegan, D. P.; Tan, C.; Daemi, S. R.; Weaving, J. S.; O'Regan, K. B.; Heenan, T. M. M.; Hinds, G.; Kendrick, E.; et al. 3D Microstructure Design of Lithium-Ion Battery Electrodes Assisted by X-Ray Nano-Computed Tomography and Modelling. *Nat. Commun.* **2020**, *11* (1), 1–13. https://doi.org/10.1038/s41467-020-15811-x.

(48) Lindström, H.; Södergren, S.; Solbrand, A.; Rensmo, H.; Hjelm, J.; Hagfeldt, A.; Lindquist, S.-E. Li^+ Ion Insertion in TiO_2 (Anatase). 2. Voltammetry on Nanoporous Films. *J. Phys. Chem. B* **1997**, *101* (39), 7717–7722. https://doi.org/10.1021/jp970490q.

(49) Augustyn, V.; Come, J.; Lowe, M. A.; Kim, J. W.; Taberna, P. L.; Tolbert, S. H.; Abruña, H. D.; Simon, P.; Dunn, B. High-Rate Electrochemical Energy Storage through Li^+ Intercalation Pseudocapacitance. *Nat. Mater.* **2013**, *12* (6), 518–522. https://doi.org/10.1038/nmat3601.

(50) Liu, T.-C.; Pell, W. G.; Conway, B. E.; Roberson, S. L. Behavior of Molybdenum Nitrides as Materials for Electrochemical Capacitors. *J. Electrochem. Soc.* **1998**, *145* (6), 1882–1888. https://doi.org/10.1149/1.1838571.

(51) Wang, J.; Polleux, J.; Lim, J.; Dunn, B. Pseudocapacitive Contributions to Electrochemical Energy Storage in TiO_2 (Anatase) Nanoparticles. *J. Phys. Chem. C* **2007**, *111* (40), 14925–14931. https://doi.org/10.1021/jp074464w.

(52) Ko, J. S.; Sassin, M. B.; Rolison, D. R.; Long, J. W. Deconvolving Double-Layer, Pseudocapacitance, and Battery-like Charge-Storage Mechanisms in Nanoscale $LiMn_2O_4$ at 3D Carbon Architectures. *Electrochim. Acta* **2018**, *275*, 225–235. https://doi.org/10.1016/j.electacta.2018.04.149.

(53) Julien, C.; Mauger, A.; Vijh, A.; Zaghib, K. *Lithium Batteries: Science and Technology*; Springer

International Publishing: New York, 2016.

(54) Tian, R.; Park, S. H.; King, P. J.; Cunningham, G.; Coelho, J.; Nicolosi, V.; Coleman, J. N. Quantifying the Factors Limiting Rate Performance in Battery Electrodes. *Nat. Commun.* **2019**, *10* (1). https://doi.org/10.1038/s41467-019-09792-9.

(55) Huang, J.; Li, Z.; Zhang, J.; Song, S.; Lou, Z.; Wu, N. An Analytical Three-Scale Impedance Model for Porous Electrode with Agglomerates in Lithium-Ion Batteries. *J. Electrochem. Soc.* **2015**, *162* (4), A585–A595. https://doi.org/10.1149/2.0241504jes.

(56) Tsumura, T.; Inagaki, M. Lithium Insertion/Extraction Reaction on Crystalline MoO_3. *Solid State Ionics* **1997**, *104* (3–4), 183–189. https://doi.org/10.1016/s0167-2738(97)00418-9.

(57) Kim, H.-S.; Cook, J. B.; Lin, H.; Ko, J. S.; Tolbert, S. H.; Ozolins, V.; Dunn, B. Oxygen Vacancies Enhance Pseudocapacitive Charge Storage Properties of MoO_{3-x}. *Nat. Mater.* **2017**, *16* (4), 454–460. https://doi.org/10.1038/nmat4810.

(58) Li, W.; Cheng, F.; Tao, Z.; Chen, J. Vapor-Transportation Preparation and Reversible Lithium Intercalation/Deintercalation of α-MoO_3 Microrods. *J. Phys. Chem. B* **2006**, *110* (1), 119–124. https://doi.org/10.1021/jp0553784.

(59) Besenhard, J.; Heydecke, J.; Fritz, H. Characteristics of Molybdenum Oxide and Chromium Oxide Cathodes in Primary and Secondary Organic Electrolyte Lithium Batteries I. Morphology, Structure and Their Changes during Discharge and Cycling. *Solid State Ionics* **1982**, *6* (3), 215–224. https://doi.org/10.1016/0167-2738(82)90042-X.

(60) Wustrow, A.; Hancock, J. C.; Incorvati, J. T.; Vaughey, J. T.; Poeppelmeier, K. R. Effect of Fluoride Doping on Lithium Diffusivity in Layered Molybdenum Oxide. *ACS Appl. Energy Mater.* **2019**, *2* (3), 2080–2086. https://doi.org/10.1021/acsaem.8b02141.

(61) Yu, M.; Shao, H.; Wang, G.; Yang, F.; Liang, C.; Rozier, P.; Wang, C. Z.; Lu, X.; Simon, P.; Feng, X. Interlayer Gap Widened *α*-Phase Molybdenum Trioxide as High-Rate Anodes for Dual-Ion-Intercalation Energy Storage Devices. *Nat. Commun.* **2020**, *11* (1), 1–9. https://doi.org/10.1038/s41467-020-15216-w.

(62) Wang, B.; Ang, E. H.; Yang, Y.; Zhang, Y.; Geng, H.; Ye, M.; Li, C. C. Interlayer Engineering of Molybdenum Trioxide toward High-Capacity and Stable Sodium Ion Half/Full Batteries. *Adv. Funct. Mater.* **2020**, *30* (28), 1–11. https://doi.org/10.1002/adfm.202001708.

(63) Zhang, H.; Wu, W.; Liu, Q.; Yang, F.; Shi, X.; Liu, X.; Yu, M.; Lu, X. Interlayer Engineering of *α*-MoO_3 Modulates Selective Hydronium Intercalation in Neutral Aqueous Electrolyte. *Angew. Chemie - Int. Ed.* **2021**, *60* (2), 896–903. https://doi.org/10.1002/anie.202010073.

(64) Hu, Z.; Zhang, X.; Peng, C.; Lei, G.; Li, Z. Pre-Intercalation of Potassium to Improve the Electrochemical Performance of Carbon-Coated MoO_3 Cathode Materials for Lithium Batteries. *J. Alloys Compd.* **2020**, *826*, 154055. https://doi.org/10.1016/j.jallcom.2020.154055.

(65) Gallagher, K. G.; Trask, S. E.; Bauer, C.; Woehrle, T.; Lux, S. F.; Tschech, M.; Lamp, P.; Polzin, B. J.; Ha, S.; Long, B.; et al. Optimizing Areal Capacities through Understanding the Limitations of Lithium-Ion Electrodes. *J. Electrochem. Soc.* **2016**, *163* (2), A138–A149. https://doi.org/10.1149/2.0321602jes.

(66) Fleischmann, S.; Zeiger, M.; Quade, A.; Kruth, A.; Presser, V. Atomic Layer-Deposited Molybdenum Oxide/Carbon Nanotube Hybrid Electrodes: The Influence of Crystal Structure on Lithium-Ion Capacitor Performance. *ACS Appl. Mater. Interfaces* **2018**, *10* (22), 18675–18684. https://doi.org/10.1021/acsami.8b03233.

(67) Xu, Y.; Xuan, H.; Gao, J.; Liang, T.; Han, X.; Yang, J.; Zhang, Y.; Li, H.; Han, P.; Du, Y. Hierarchical Three-Dimensional $NiMoO_4$-Anchored RGO/Ni Foam as Advanced Electrode Material with Improved Supercapacitor Performance. *J. Mater. Sci.* **2018**, *53* (11), 8483–8498. https://doi.org/10.1007/s10853-018-2171-1.

(68) Xia, X.; Chao, D.; Ng, C. F.; Lin, J.; Fan, Z.; Zhang, H.; Shen, Z. X.; Fan, H. J. VO_2 Nanoflake Arrays for Supercapacitor and Li-Ion Battery Electrodes: Performance Enhancement by Hydrogen Molybdenum Bronze as an Efficient Shell Material. *Mater. Horizons* **2015**, *2* (2), 237–244. https://doi.org/10.1039/C4MH00212A.

(69) Wu, C.; Zhu, Y.; Ding, M.; Jia, C.; Zhang, K. Fabrication of Plate-like MnO_2 with Excellent Cycle

Stability for Supercapacitor Electrodes. *Electrochim. Acta* **2018**, *291*, 249–255. https://doi.org/10.1016/j.electacta.2018.08.126.

(70) Yao, B.; Chandrasekaran, S.; Zhang, J.; Xiao, W.; Qian, F.; Zhu, C.; Duoss, E. B.; Spadaccini, C. M.; Worsley, M. A.; Li, Y. Efficient 3D Printed Pseudocapacitive Electrodes with Ultrahigh MnO_2 Loading. *Joule* **2019**, *3* (2), 459–470. https://doi.org/10.1016/j.joule.2018.09.020.

3D deterministic electrode architectures were fabricated using a scalable, room-temperature electrodeposition protocol to coat free-standing, aligned CNT foams with molybdenum trioxide. This general electrode design approach that provided well-distributed electron and ion transport pathways led to high areal and volumetric capacities and good rate performance for electrochemical energy storage.

Keyword: batteries

TOC Graphic